PHYSICAL REVIEW B **106**, 184110 (2022)

Fingerprints of carbon defects in vibrational spectra of GaN considering the isotope effect

I. Gamov,[1,*] J. L. Lyons,[2] G. Gärtner,[3] K. Irmscher,[1] E. Richter,[4] M. Weyers,[4]
M. R. Wagner,[5,6] and M. Bickermann[1]
[1]*Leibniz-Institut für Kristallzüchtung (IKZ), Berlin, Germany*
[2]*Center for Computational Materials Science, United States Naval Research Laboratory (NRL), Washington, DC, USA*
[3]*Institute of Experimental Physics, TU Bergakademie Freiberg, Freiberg, Germany*
[4]*Ferdinand-Braun-Institut (FBH), Berlin, Germany*
[5]*Technische Universität Berlin, Institute of Solid State Physics, Berlin, Germany*
[6]*Paul-Drude-Institut für Festkörperelektronik, Leibniz-Institut im Forschungsverbund Berlin e.V., Berlin, Germany*

(Received 26 September 2022; revised 3 November 2022; accepted 8 November 2022; published 29 November 2022)

In this paper, we examine the carbon defects associated with peaks of infrared (IR) absorption and Raman scattering appearing in GaN crystals at carbon (^{12}C) doping in the range of concentrations from 3.2×10^{17} to 3.5×10^{19} cm^{-3}. Here, 14 unique vibrational modes of defects are observed in GaN samples grown by HVPE (hydride vapor phase epitaxy) and then compared with defect properties predicted from first-principles calculations. The vibrational frequency shift in two ^{13}C-enriched samples related to the effect of the isotope mass indicates six distinct configurations of the carbon-containing point defects. The effect of the isotope replacement is well reproduced by the density functional theory (DFT) calculations. Specific attention is paid to the most pronounced defects, namely, tricarbon complexes ($C_N{=}C{=}C_N$) and carbon substituting for nitrogen (C_N). The position of the transition level $(+/0)$ in the bandgap found for $C_N{=}C{=}C_N$ defects by DFT at 1.1 eV above the valence band maximum suggests that $(C_N{=}C{=}C_N)^+$ provides compensation of C_N^-. Here, $C_N{=}C{=}C_N$ defects are observed to be prominent yet have high formation energies in DFT calculations. Regarding C_N defects, it is shown that the host Ga and N atoms are involved in the delocalized vibrations of the defect and significantly affect the isotopic frequency shift. Much more faint vibrational modes are found from di-atomic carbon-carbon and carbon-hydrogen (C–H) complexes. Also, we note changes of vibrational mode intensities of C_N, $C_N{=}C{=}C_N$, C–H, and C_N–C_i defects in the IR absorption spectra upon irradiation in the defect-related ultraviolet/visible absorption range. Finally, it is demonstrated that the resonant enhancement of the Raman process in the range of defect absorption >2.5 eV enables the detection of defects at carbon doping concentrations as low as 3.2×10^{17} cm^{-3}.

DOI: 10.1103/PhysRevB.106.184110

I. INTRODUCTION

Carbon is a common contaminant in the epitaxy of GaN crystals as well as an intentional dopant in GaN-based high-power device technologies. It is frequently used to achieve semi-insulating substrates and buffer layers [1–6]. In *n*-type GaN, carbon doping leads to the formation of compensating acceptors, in which a single carbon atom substitutes for a nitrogen host atom (C_N) [7–10]. This defect is usually considered the prevailing carbon defect in *n*-type GaN due to its low formation energy [11–17]. A deep acceptor level $(0/-)$ of C_N defect is expected from theoretical consideration at ~0.9 eV above the valence band maximum (VBM). It is in good agreement with the zero phonon line (ZPL) at 0.92 eV observed in photoluminescence (PL) spectra as well as deep-level transient spectroscopy (DLTS) data, high-temperature conductivity, bulk photovoltaic effect, and charge transfer processes observed in GaN:C [12,18–20]. Further PL and DLTS studies have supported the finding that there is a $(+/0)$ level of C_N that can act as a hole trap, compensating Mg doping in *p*-type GaN [12,21]. Two intense infrared (IR) absorption bands appearing at 1678 and 1718 cm^{-1} in GaN:C samples were interpreted as antisymmetric vibrational modes (ν_3) of tricarbon (TC) defects [22,23] and correlate with a characteristic red PL band [24]. However, these defects are distinct from the carbon complexes in theoretical reports [10,14,16], and hence, the role of the observed TC defects in the charge balance is not yet understood.

Often carbon is described as an amphoteric impurity because of its propensity to act as an acceptor or donor depending on the underlying conditions. Among the defects reported in theoretical works are carbon substituting the gallium site (C_{Ga}), different configurations of interstitial carbon (C_i), carbon pairs (such as C_{Ga}–C_N or C_N–C_i), as well as various carbon-containing complexes with intrinsic defects or other impurities such as hydrogen, oxygen, or silicon. Thus, the ability of carbon to form stable bonds with Ga, N, and other C atoms results in a huge variety of possible stable point defects [9,14–16]. Some of these defects can play the role of donors and compensate or passivate acceptor doping.

---

[*] Present address: Technische Physik, University of Würzburg, Würzburg, Germany; ivan.gamov@uni-wuerzburg.de

Hence, the identification of the most common types of carbon-containing defects and their properties is of paramount importance and a critical step in understanding the electrical properties of carbon-doped GaN [10,13–15,25]. Moreover, as we will show, a high defect formation energy does not necessarily contradict the high density of such defects.

In this paper, we identify various carbon-related defects by combining methods of vibrational spectroscopy with calculations of the defect structure, vibrational frequencies, and atomic displacements using density functional theory (DFT). Comprehensive IR absorption and Raman studies of GaN samples doped with different carbon isotopes (GaN:C) are conducted to identify the spectroscopic fingerprints of the different carbon-based point defects in GaN. A series of eight ^{12}C-doped GaN samples with varying doping concentration $[C] = [^{12}C] + [^{13}C]$ between 3.2×10^{17} and 3.5×10^{19} cm^{-3} and natural isotope ^{13}C abundance 1.1% were grown to investigate the vibrational frequencies of the carbon point defects. In two additional samples with elevated concentration of the ^{13}C isotope, we observe a change of the vibrational frequencies of several peaks caused by C doping. The analysis of the isotopic splitting via the harmonic oscillator approximation enables the identification of one, two, or three carbon atoms in the corresponding defect structure. Independent computation by DFT specified the structure of defects which could vibrate at these frequencies and clarified possible vibrational modes. We identify the origin of the recently observed vibrational modes at 765 and 774 cm^{-1} [11,26,27]. We unravel a correlation with two additional vibrational modes related to the same defect center and present a defect model explaining all four vibrational modes and their ^{13}C-related replicas. Moreover, based on first-principles calculations, we establish the structure of TC defects responsible for the intense IR absorption and calculate their charge states in the bandgap [22,23]. Finally, we consider several hitherto unnoticed peaks of IR absorption (carbon-hydrogen and carbon pairs) and demonstrate changes in the IR absorption intensity of most defect types under additional excitation at photon energies below the bandgap energy (2.71 and 3.22 eV). We also demonstrate methods to recognize the appearance of both C_N and $C_N{=}C{=}C_N$ at carbon doping concentrations as low as 3.2×10^{17} cm^{-3}.

II. MATERIALS AND METHODS

Ga-polar *c*-plane-oriented GaN layers, undoped or doped by carbon with natural or varied isotope composition, were grown by hydride vapor phase epitaxy (HVPE) on 2-inch (0001) GaN/sapphire templates. The growth and doping procedure is described in detail in Ref. [18]. The sources of carbon doping were liquid pentane (Dockweiler Chemicals, electronic grade) or gaseous butane [Sigma Aldrich, Butane 12C4 (Gas) 99%] containing carbon in the natural isotopic composition, and gaseous butane isotopically enriched with ^{13}C to 99% [Sigma Aldrich, Butane 13C4 (Gas) 99%], which was used to achieve carbon doping with 99% and 50% fraction of the isotope ^{13}C. All layers separated from the sapphire substrates spontaneously after cooldown due to the large difference of thermal expansion coefficients. The *c*-plane-oriented samples, with areas of $\sim 10 \times 5$ mm^2 and 0.5–1 mm thickness, were diced, and both *c* faces were polished. From two samples (GaN140 and GaN051-50; sample descriptions are provided below), cross-sectional *m*-plane stripes of $\sim 5 \times 1 \times 0.5$ mm^3 were cut and polished. Concerning the crystalline perfection of the samples, we refer to the detailed investigation reported recently [18]. In-plane and out-of-plane strain of the *c*-plane GaN layers are negligible (the accuracy of the measurement of the lattice constants by x-ray diffraction was ±0.03 and ±0.01%, respectively), and the full width at half maximum of x-ray diffraction rocking curves at the symmetric (002) reflection and the skew symmetric (302) reflection vary between 80 and 120 arcsec. The results of these measurements are essentially independent of whether the layers are carbon doped or not, indicating that carbon doping does not impair the crystalline quality. The positions of the strain-related intrinsic Raman scattering bands only insignificantly differ and do not correlate with [C].

TABLE I. Chemical concentrations of carbon isotopes and hydrogen in samples obtained by SIMS.

Sample name	$[C] = [^{12}C] + [^{13}C]$ 10^{17} cm^{-3}	$[^{13}C]/[C]$	[H] 10^{17} cm^{-3}	Precursor
GaN000	<0.24	1%	1	–
GaN003	3.2	1%		Pentane
GaN005	5.0	1%		Pentane
GaN019	19	1%		Pentane
GaN058	58	1%		Pentane
GaN090	90	1%	6	Pentane
GaN140	140	1%		Pentane
GaN300	300	1%		Pentane
GaN350	350	1%	8	Pentane
GaN051-50[a]	51	50%		Butane
GaN025-99[b]	25	99%		Butane

[a] Sample denoted as C1213 in Ref. [22].

[b] Sample denoted as C13 in Ref. [22].

The chemical concentrations of carbon, oxygen, silicon, and hydrogen in the GaN layers were determined by secondary ion mass spectrometry (SIMS; performed by RTG Mikroanalyse GmbH Berlin). The numbers in the sample name indicate the value of [C] in units of 10^{17} cm^{-3} (as given in Table I). In the undoped reference sample, [C], [O], and [Si] are below the respective SIMS detection limits: $[C] < 2.4 \times 10^{16}$ cm^{-3}, $[O] < 2 \times 10^{16}$ cm^{-3}, and $[Si] < 7 \times 10^{15}$ cm^{-3}. In the samples doped from pentane, the measured [O] and [Si] are slightly above corresponding detection limits and equal to 3.5×10^{16} and 1.3×10^{16} cm^{-3}, respectively, while in the samples doped from isotopically enriched butane, [O] reaches 3.5×10^{17} cm^{-3}. Here, [H] is at $\sim \times 10^{17}$ cm^{-3} for undoped GaN layers and does not exceed 8×10^{17} cm^{-3} for any carbon doping level in this paper. Two samples, GaN051-50 and GaN025-99, have been doped with a significant fraction of ^{13}C; the fraction (50%, 99%) is denoted as the second number in the sample name. The total carbon concentration [C] and the respective ^{13}C percentage of each sample $[^{13}C]/[C]$ are specified in Table I. Comparing [C] with the residual impurity concentrations mentioned above, [O] and [Si] attain at most $\frac{1}{10}$ of [C], while [H] never exceeds $\frac{1}{3}$. Hence, compensation or passivation of carbon acceptors by these impurities is not expected to play a major role in this paper.

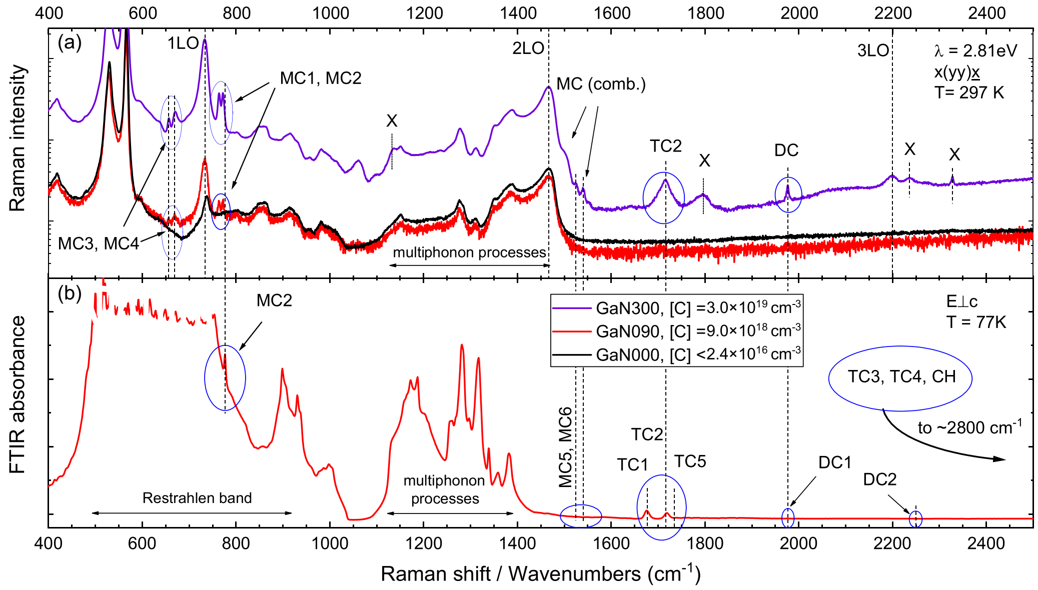

FIG. 1. Overview of carbon defect vibrational modes in GaN:C. (a) The room temperature Raman spectra are shown for the reference carbon-free sample ([C] $< 2.4 \times 10^{16}$ cm^{-3}) and two C-doped samples GaN090 and GaN300 at 2.81 eV excitation energy and $x(yy)\underline{x}$ geometry. (b) The absorption spectrum of sample GaN090 is taken at $E \perp c$ polarization and a temperature of 77 K. Peaks labeled: monocarbon (MC), dicarbon (DC), and tricarbon (TC) are related to carbon-defects of different groups, LO indicates longitudinal optical phonon modes, and X indicates peaks of unclear origin. The peaks TC3, TC4, and carbon-hydrogen (CH) in the range of 2670–2850 cm^{-1} are shown in Fig. 5(b).

Fourier transform infrared (FTIR) absorption measurements were performed in the midinfrared spectral range on a Bruker Vertex 80v spectrometer equipped with a globar source, a potassium bromide beam splitter, and a liquid nitrogen cooled mercury cadmium telluride detector at different temperatures. For measurements below room temperature (RT), a liquid-helium-flow cryostat (Oxford OptistatCF) with zinc selenide windows was used. The spectra were recorded with a resolution of 0.5 cm^{-1} at RT and 0.25 cm^{-1} at 10 K. For polarization-dependent measurements, a holographic wire grid polarizer on a KRS-5 substrate was used. Additional FTIR measurements were carried out under below-bandgap illumination. The exciting light of wavelength 385 nm (3.22 eV) or 455 nm (2.71 eV) was guided by an optical fiber from a power light-emmitting-diode source (Omicron LedHUB) into the sample chamber of the FTIR spectrometer using a vacuum-tight feedthrough. The fiber output was positioned in such a way that it was outside of the FTIR sample beam and that the LED divergent beam was incident under ~60° to the sample surface. Nominal LED power <3000 mW was used in a continuous mode. Additional measurements in the range of Reststrahlen band absorption were done on sample GaN090 with a Bruker Tensor 27 spectrometer and an Oxford CF 2102 cryostat with KRS5 windows at liquid nitrogen temperature (Fig. 1).

Raman experiments were carried out at RT, with incident laser light at excitation wavelengths of 2.81 and 2.41 eV (442 and 514 nm) using a Horiba LabRAM HR800 Raman microscope spectrometer. Half-wave plates suited for the visible spectral range were used to change the direction of the electric field vector E of the incident linearly polarized light from the exciting laser. The outgoing backscattered light was guided through a linear polarizer (analyzer). The orientation of the light beam and the polarization directions in the coordinate system of the GaN crystal ($z \parallel c$, $x \perp c$, $y \perp c$, and $x \perp y$) are defined using the Porto notation: $k(e_1 e_2)\underline{k}$, where k and $\underline{k}$ are the antiparallel directions of incoming and outgoing scattered light propagation, while e_1 and e_2 determine the orientation of electric field vector $\vec{E}$ of incoming and scattered light, respectively.

The methodology for DFT calculations is the same as in Ref. [10], which is outlined in more detail in Ref. [28]. Projector-augmented wave pseudopotentials [29] are used within the VASP code [30], and the HSE hybrid functional [31,32] is employed to provide a correct description of the bandgap and defect properties. Here, 96-atom supercells are used with a 400 eV cutoff. Defect vibrational modes are calculated using the finite-difference method within VASP, and isotope effects are explored by adjusting atomic masses before recalculating the Hessian matrix. Two shells of atoms are included in the vibrational mode calculations (i.e., nearest neighbors as well as next-nearest neighbors); as will be seen below, this is important for obtaining relevant modes for C_N.

III. RESULTS AND DISCUSSION

The broad-range spectra of Raman scattering at RT (a) and IR absorption at 77 K (b) are shown in Fig. 1. Raman spectra in Fig. 1(a) of the undoped reference sample (black solid line) and two different C-doped GaN crystals reproduce similar general spectral features originating from intrinsic vibrations. The peaks at 532 and 567 cm^{-1} are identified as intrinsic vibrational modes A_1(TO) and E_2(high) of the GaN lattice allowed for the selected polarization geometry $x(yy)x$ [33–35]. The mode E_1(LO) at 741 cm^{-1} has the highest frequency within the first-order phonon spectrum of GaN, thus limiting the range of *intrinsic* first-order Raman modes (labeled 1LO). Naturally, the 2LO and 3LO frequencies define the ranges of second- and third-order intrinsic vibrations, respectively. Multiphonon processes are clearly visible in the second-order range between 1LO and 2LO. Accordingly, the IR absorption spectrum of sample GaN090 [Fig. 1(b)] contains signals in the range 1100–1500 cm^{-1} caused by two-phonon processes, while the opacity at lower wave numbers corresponds to the Restrahlen band [36].

Apart from the first- and higher-order host lattice vibrations, additional peaks of carbon-related defect vibrational modes appear in the C-doped spectra in Fig. 1. They are marked by blue circles. Labels monocarbon (MC), dicarbon (DC), and TC group the peaks for further discussion, where individual peaks are labeled with additional numbering (TC1, DC2, etc.). The exact peak positions are shown in the summarizing table in Sec. III D. Peaks labeled with X are of unknown origin and not further discussed within this paper.

To unravel the defect structure related to the observed vibrational signatures, we investigate the isotope effect in carbon-doped samples with controlled ^{12}C and ^{13}C doping and analyze the frequency shifts within the harmonic oscillator approximation. The vibrational frequency ν of the oscillator given in wave numbers (cm^{-1}) is determined by the masses of vibrating atoms (m_i) and the stiffnesses of the chemical bonds. These two parameters also determine the amplitude of vibration. The replacement of a carbon atom by another isotope preserves (at least for carbon and heavier atoms, the change is insignificant) the chemical stiffness (and hence the oscillator energy) but provides a change of ν and vibrational amplitudes of the system due to the change of atomic mass ($m \rightarrow m^*$). The relative frequency shift is expressed by frequency ratio $f \equiv \frac{\nu}{\nu^*}$.

It should be noted that the impact of the individual atom to the change of vibrational frequency is proportional to the amplitude of its vibration squared. In the special case of a vibration involving only two mobile atoms ($i = 2$), replacing $m_1, m_2 \rightarrow m_1^*, m_2^*$ results in the frequency ratio:

$$\frac{\nu}{\nu^*} = \left[\frac{m_1^* m_2^* (m_1 + m_2)}{m_1 m_2 (m_1^* + m_2^*)}\right]^{0.5}. \tag{1}$$

When both vibrating atoms are ^{12}C and replaced by ^{13}C, the frequency ratio reaches the theoretical maximum $f_{\max} \approx 1.041$ for carbon atoms. Note that this is a constant value, actual not only for the simplest case of the diatomic oscillator but also for any vibrating defects when all n carbon atoms with nonzero vibrational amplitude are replaced and there are no other vibrating atoms in the defect structure [22,37]. The mobile but unreplaced atoms, e.g., some carbon atoms at mixed $^{12}\text{C} + {}^{13}\text{C}$ doping or nitrogen atoms in C-C-N and N-C-N chainlike defects in GaAs, result in frequency ratio f significantly smaller than $f_{\max}$ [38,39]. Furthermore, host atoms around the defect, being involved in the vibrational mode, impact the vibrational mode in the same manner, decreasing f. In this paper, we use DFT to evaluate the impact of host atoms on the value of the frequency ratio f that becomes critically important for certain vibrational modes of C_N acceptors because these modes exhibit host-atom involvement.

The number of carbon atoms in the defect structure is determined by the splitting of the original vibrational mode frequency in the sample with equal concentrations of two isotopes (GaN051-50) due to the maximum diversity of isotopomers, i.e., defects different only in the isotope composition. One can distinguish three groups of isotopomers: ^{12}C-pure and ^{13}C-pure containing only ^{12}C or ^{13}C atoms, respectively, and mix isotopomers containing both isotopes, in this sample. At $[^{12}\text{C}] = [^{13}\text{C}] = 50\%$, all N isotopomers become statistically equivalent, and hence, they are present in equal quantity in the vibrational spectra. Then the number of isotopomers $N = 2^n$ is equal to the number of combinations of two isotopes on n sites of carbon atoms in the defect structure. The number of unique frequencies in this case is $\leqslant 2^n$, considering degeneracies of structurally equivalent isotopomers of symmetrical defects [22].

More information about the structure can be obtained from the measurements of IR absorption polarization. The IR absorption of the vibrating dipole $\Delta\vec{\mu}$ of a defect vibrational mode in a crystal is maximum when $\Delta\vec{\mu} \parallel \vec{E}$ and zero at $\Delta\vec{\mu} \perp \vec{E}$. The absorption $A(\varphi, \gamma)$ as a function of the angles γ (the tilt angle between $\Delta\vec{\mu}$ and wurtzite symmetry axis c) and φ (between $\vec{E}$ and c) can be expressed by the equation considering the symmetry properties of GaN crystals [40]:

$$A(\varphi, \gamma) = A_0[\sin^2\gamma + (2 - 3\sin^2\gamma)\cos^2\varphi], \tag{2}$$

where A_0 is the normalization constant. From this equation, the orientation of a defect can be found by just two measurements of the linearly polarized absorption coefficient at $E \parallel c (\varphi = 0^\circ)$ and $E \perp c (\varphi = 90^\circ)$:

$$P = \frac{A(90, \gamma)}{A(0, \gamma)}, \quad \gamma = \arcsin\left(\frac{2}{2+P}\right)^{1/2}. \tag{3}$$

Following the previous discussion on the general aspects of the isotope effect in vibrational spectroscopy of carbon-doped GaN, the subsequent sections focus on the identification of specific MC, DC, and TC defect complexes.

A. MC defects and CH modes

1. Vibrations of C_N *defect*

Figure 2 shows the Raman spectra of the reference GaN (dashed) and 6 GaN:C samples with different carbon concentrations between 5×10^{17} and 3×10^{19} cm^{-3} in the spectral range between 640 and 790 cm^{-1}. Since the Reststrahlen band blocks IR transmission between 600 and 800 cm^{-1} [Fig. 1(b)], Raman scattering is the preferable method for investigating defect vibrations in this range. Apart from the dominating host GaN lattice modes A_1(LO) and E_1(LO), four well-separated peaks can be identified whose intensity increases with increasing carbon doping. These four scattering peaks MC1–MC4 (see Table II) are recognized vibrations of carbon-based defects. They become very intense at high [C] and have proportional integrated area, as shown in Fig. 2(b) for the most accurate measurements (at [C] $> 1.9 \times 10^{18}$ cm^{-3}). Scattering peaks with frequencies close to true MC3, MC4 (655–670 cm^{-1}) [41–44] are often observed independently on the other MC peaks at the doping with Mn, Mg, or the implantation of different atoms. As will

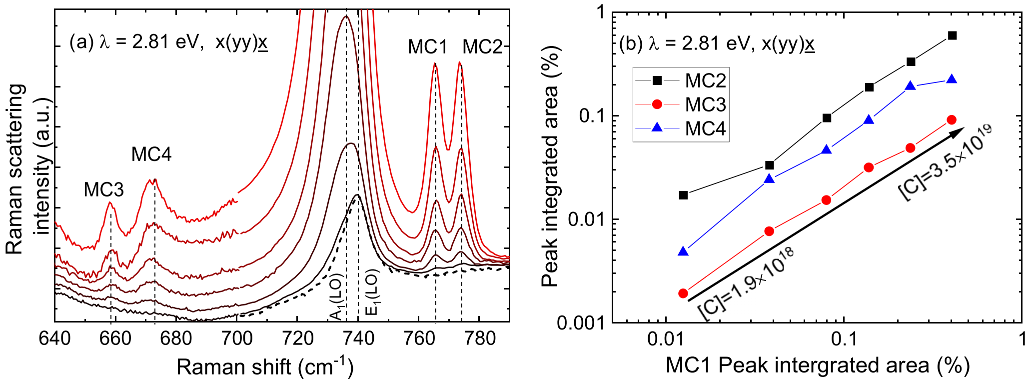

FIG. 2. (a) Raman scattering spectra of samples at [C] in the range from 5×10^{17} to 3×10^{19} cm^{-3} measured on the *m* facet of *c*-plane wafers in the $x(yy)\underline{x}$ geometry at room temperatures. The individual spectral curves are normalized to the integrated area in the range from 150 to 1535 cm^{-1}. (b) The corresponding integrated peak area for vibrational modes MC1–MC4 for the samples at [C] = 1.9×10^{18} cm^{-3} and above.

be shown below, the nature of the MC3, MC4 vibrations are highly determined by the GaN lattice, while the influence of the impurity atom on the vibration frequency is of secondary importance for the considered carbon defect. In this respect, the true MC3, MC4 modes should not be confused with other peaks and must be considered only as a part of the group. The four always proportional scattering peaks MC1–MC4 provides reliable agreement with the model of only one type of substitutional C defect considered by DFT.

Within the calculated (most expected) defects with only one carbon atom in the structure (C_{Ga}, C_N, and C_i in Table II), only C_N in the negative charge state (C_N^-) [Figs. 3(a)–3(d)] possesses four vibrational frequencies close to the optical phonon band and explains all four peaks MC1–MC4 simultaneously including their polarization properties. In contrast, C_{Ga} and C_i defects possess too different vibrational frequencies to associate them with the peaks MC1–MC4. A mode ∼785 cm^{-1} and a doubly degenerate mode ∼775 cm^{-1} were found by DFT previously [10]. As shown in Figs. 3(a) and 3(b), these modes are dominated by displacements of the C impurity atom. The two further modes found for C_N^- are doubly degenerate modes at 662 and 655 cm^{-1}. These modes were not observed in earlier reports, as the nearest in-phase nitrogen shells were not used to construct the Hessian matrix [10,11]. The character of these modes can be seen in Figs. 3(c) and 3(d). Unlike the highest wave number modes, these modes have only weak carbon character due to many in-phase vibrating nitrogen atoms located around C_N. In Fig. 3(e), there are the spectral curves of sample GaN140 for five different geometries captured from the facet [i.e., geometries $x(zz)x$, $x(zy)x$, and $x(yy)x$] or from the *c* plane [i.e., geometries $z(xx)z$ and $z(xy)z$]. Based on these spectra, the *A* and *E* symmetry of the MC1–MC4 modes is derived in accordance with Raman selection rules, as indicated in the labels in Fig. 3(e). In this respect, explaining modes MC1–MC4, we exclude the other defects with one carbon atom. Utilizing the isotope effect, we show below that defects with more than one carbon atom can also be excluded.

Table II represents the isotopic shifts of vibrational frequencies (as frequency ratio *f*) due to substituting ^{13}C for ^{12}C in DFT calculations for three different types of MC defects, C_N, C_{Ga}, and C_i. MC3 and MC4 vibrational modes belong to the range of frequencies propagating in GaN crystals (the vibrational band formed by the optical phonon branches). The specifics of this case, also known as the band mode, are that the major part of the vibrational energy is stored in the vibrational displacement of many host atoms of the crystal. Thus, a change in the mass of the impurity atom during isotopic replacement does not affect the oscillation frequency. Modes 662 and 655 cm^{-1} satisfy this condition, and DFT calculations provide <1 cm^{-1} shift for the modes ($f = 1.00$) for the supercells considered here. MC1 and MC2 modes, having vibrational frequencies near the range of allowed vibrations, are also influenced by the host atoms. We find that the frequency shift to lower wave numbers depends on the number of the host atoms considered in the model. An increase in the number of gallium and nitrogen atoms reduces the relative impact of the carbon atom, leading to a decrease of *f* from 1.036 (1 carbon and 3 neighboring Ga atoms) to 1.030 (3 Ga-N shells around C atom). In contrast, changing

TABLE II. The vibrational frequencies found from the Raman spectra and calculated via DFT for different models of defects C_N, C_{Ga}, and C_i.

Experiment		DFT					
^{12}C, cm^{-1}	*f*	$^{12}C_N^-$, cm^{-1}	*f*	$^{12}C_{Ga}^+$, cm^{-1}	*f*	$^{12}C_i^0$, cm^{-1}	*f*
766 (MC1)	1.028	775	1.030	843	1.027	1511	1.021
774 (MC2)	1.028	785	1.030	836	1.026	734	1.027
659 (MC3)	1.000	655	1.00	831	1.026	727	1.009
672 (MC4)	1.000	662	1.00	735	1.000	466	1.015

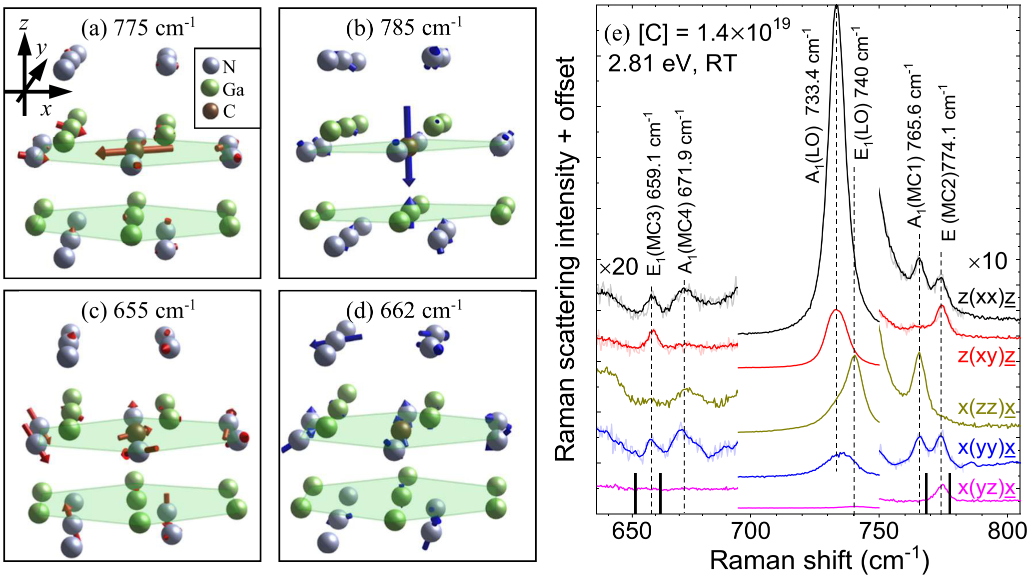

FIG. 3. (a)–(d) Displacements of atoms (shown by arrows) according to density functional theory (DFT) calculations in the four vibrational modes of the C_N defect are found at vibrational frequencies 775, 785, 655, and 662 cm^{-1}. The frequencies can be associated with modes MC1–MC4, respectively, presented in Raman spectra (e) by stick spectra.

the number of neighboring atoms gives no visible effect for the localized vibrational modes of C_{Ga} and C_i.

Isotopic shifts of $f = 1.00$ (MC3, MC4) and $f = 1.028$ (MC1, MC2) are demonstrated in Fig. 4. The vibrational frequencies of the MC1 and MC2 modes associated with ^{12}C isotopes (black line) are 766 and 774 cm^{-1}. Geometries $x(yy)x$ and $x(yz)x$ allow us to distinguish between these two modes. Accordingly, the two peaks with similar polarization properties appear in both samples with an elevated abundance of ^{13}C isotopes at a lower frequency of vibration (745 and 753 cm^{-1}, respectively), resulting in $f = 1.028$ for both the MC1 and MC2 modes. The ^{13}C-related pair of peaks is exclusively observed in samples with significant concentrations of ^{13}C and associated with the ^{13}C pure isotopomers of the corresponding defects. It is also important to note that, for the GaN051-50 sample, there are no additional peaks between the ^{13}C and ^{12}C peaks that would be associated with the mixed isotopomers of possible multicarbon defects. Thus, the double splitting of each of the MC1 and MC2 modes indicates the involvement of a defect with one C atom. The frequencies of the band modes MC3 and MC4 do not change in ^{13}C-enriched samples for the reasons mentioned above. Since the number of vibrating host atoms is much larger in the real crystal, the experimental value $f = 1.028$ for modes MC1 and MC2 is slightly smaller than the theoretical value, as expected.

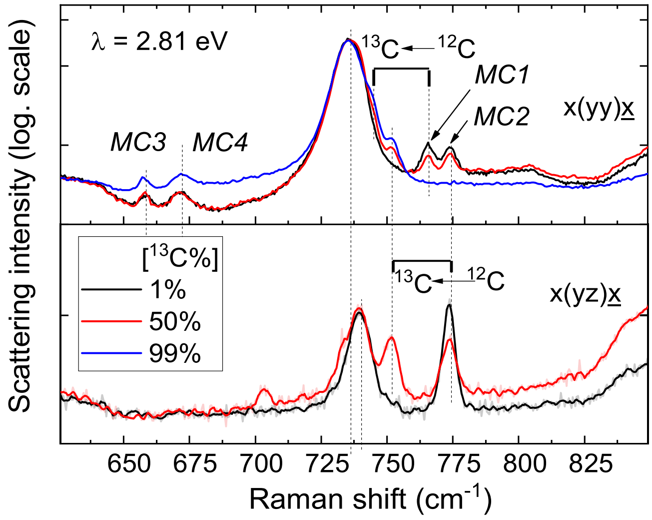

FIG. 4. Raman scattering spectra of samples with different isotope abundance [^{13}C%] equal to 1% (GaN019), 50% (GaN051-50), and 99% (GaN025-99) at 2.81 eV excitation for two different geometries of scattering, $x(yy)\underline{x}$ and $x(yz)\underline{x}$, available from the facet of the c-plane wafers [normalized to the intrinsic longitudinal optical (LO) peak height].

We also report two faint vibrational modes MC5 and MC6 appearing in the IR absorption spectra at 1539 and 1547 cm^{-1} at RT (1544 and 1553 cm^{-1} at 10 K) for $E \perp c$ polarization. The ^{13}C-related modes are observed at 1501 and 1510 cm^{-1} in both samples GaN025-99 and GaN051-50 also without additional peaks of mixed isotopomers in the sample GaN051-50. We note that a mode exactly equal to 1539 cm^{-1} was predicted previously for C_i^0 [10]. Nevertheless, DFT calculations indicate that the isotopic effect for the C_i mode is expected to be $f = 1.021$, significantly lower than the experimental value $f = 1.0285 \pm 0.0005$ (the same as for MC1 and MC2).

The exact match of f allows us to identify the peaks MC5 and MC6 as the second-order harmonic of the MC2 vibration observed in the IR absorption spectra at $E \perp c$ at 774 cm^{-1} [Fig. 1(b)]. Mode MC1 does not exhibit at $E \perp c$ polarization; hence, the second-order signals are not expected either (in our measurements of IR absorption, only faint MC1 peaks were observed at $E \parallel c$). The double-headed structure of the second-order signal is not clarified in this paper. One possible explanation could be a Fermi resonance effect since the original MC2 mode is doubly degenerate.

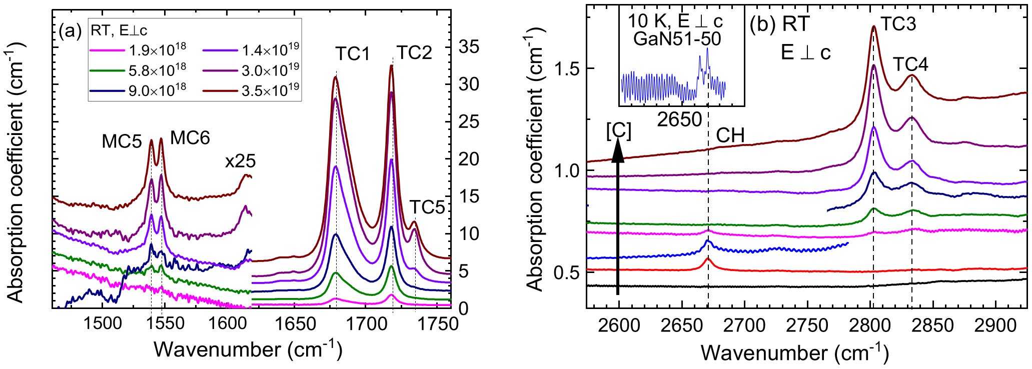

FIG. 5. (a) Infrared (IR) absorption spectra of samples with different [C] containing IR absorption peaks of monocarbon defects (MC5 and MC6) after the subtraction of the spectral curve of sample GaN005. Modes TC1 and TC2 are shown for intensity comparison. (b) IR absorption spectra of all 9 GaN samples at room temperature and polarization $E \perp c$ in the range of high wave numbers. Peaks MC5, MC6, CH, and TC1–TC5 are marked by vertical drop lines. The insert illustrates the double-splitting peak CH measured at 10 K for the same polarization in sample GaN051-50 with equal concentrations of ^{12}C and ^{13}C isotopes. See more in Fig. 10(c).

2. CH vibrations

In addition to substitutional MC on GaN host lattice sites, carbon-hydrogen vibrations can occur which are commonly observed in various semiconducting materials at high frequencies >2600 cm^{-1} [45,46]. Figure 5(b) shows the peak at 2670.3 cm^{-1} labeled CH present in samples with $[\mathrm{C}] = 1.9 \times 10^{18}$ cm^{-3} and lower near the TC3 and TC4 modes that in turn appear at higher [C]. In contrast to peaks TC3 and TC4, the CH peak splits into only two peaks in the spectra of sample GaN051-50 [see insert of Fig. 5(b)]. The peaks in this pair are close to each other ($f = 1.002$). Both peaks have the same intensity, and since there are no more peaks with that intensity in this range, only a single carbon atom is expected to be a constituent of the defect structure. According to Eq. (1), the extremely small frequency shift ($\sim$6.1 cm^{-1}) points to a neighbor of C being a very light atom (i.e., hydrogen). With $m_1 = 12$, $m_2 = m_2^* = m_\mathrm{H} = 1$, $m_1^* = 13$ *a.m.u.*, and $\upsilon_\mathrm{CH} = 2670.3$ cm^{-1}, Eq. (1) gives υ^*_CH equal to 2662.7 cm^{-1}, close to the experimental value (2664.2 cm^{-1}). The difference can be explained mostly by the deviation of the oscillator from the harmonic model. The result seems to be acceptable in comparison with the data for other semiconductors containing gallium, e.g., GaAs and GaP [45,46]. The vibrational modes for ^{12}C–H (^{13}C–H) observed at 2660.2 (2652.6) cm^{-1} and 2635.1 (2628.4) cm^{-1} have a mismatch within the harmonic model of 0.3 and 1.25 cm^{-1}, respectively [45,46]. In this way, the observations of CH isotopic shifts and the absolute frequency range are in good agreement with stretching vibrations of C–H bonds.

We have also calculated the properties of the C–H center with DFT. In this complex, C occupies a nitrogen site, and this C is directly bonded to an H atom. The electronic properties of the C–H complex are discussed in Ref. [13]. The calculated vibrational frequency is 3046 cm^{-1}, using the approach for the other complexes. However, anharmonic effects are strong for this complex. We thus employ the method outlined in Ref. [47] to obtain the anharmonic contribution. Using the approximate solution to that potential obtained from perturbation theory discussed in that reference, we find a vibrational frequency at 2794 cm^{-1}, with an anharmonic correction of 231 cm^{-1}. This is in relatively good agreement with experiment, as shown in the summarizing table in Sec. III D

B. DC defects

Following the discussion of MC and C–H vibrations, we now focus on the identification of DC defects, particularly C_i–C_N and C≡C defects. The carbon-pair defects are present in most samples but only as weak signals in the FTIR (DC1, DC2) and Raman (DC1, not shown) spectra. Figure 6(a) illustrates the intensity of the mode at RT and $E \perp c$ polarization for all 8 GaN:C samples. The isotope effect in crystals with carbon isotope abundances [^{13}C] equal to 1% (GaN058), 50% (GaN051-50), and 99% (GaN025-99) is clearly visible in Fig. 6(b) for measurements at 10 K and $E \perp c$ polarization. The similar splitting of both DC1 and DC2 modes into four individual frequencies in sample GaN051-50 indicates that two carbon atoms are present in the defect structure at two inequivalent structural positions (XY defect). In the spectra of both ^{13}C-enriched samples, ^{13}C-pure isotopomers provide vibrations at 1900.2 and 2164.2 cm^{-1}. The frequency ratio then corresponds precisely to $f_\mathrm{max} \approx 1.040 \pm 0.0005$ given by the isotope masses [22].

The range of 2000–2300 cm^{-1} corresponds to stretching vibrations of C=N, C≡N, C=C, and C≡C pairs and antisymmetric stretching vibrations of carbon and nitrogen atoms [48]. We exclude any vibrations involving noncarbon atoms (e.g., antisymmetric stretching of C=N=C or C=C = N defects) based on the observations of f_max in our cases [10,14]. According to earlier DFT calculations of the C_i–C_N defect, the carbon pair tilts by 55.8 ° relative to the c axis, providing a similar frequency of vibration (2049 or 2057 cm^{-1}) when in the + charge state [10,14], in good agreement with DC1. The dependence on polarization shown in Fig. 7 provides further evidence. According to Eq. (3), the absorption peak areas of the DC1 and DC2 peaks measured at two polarizations $E \perp c$ and $E \parallel c$ provide the values of the tilt angles as $\sim$55° and 30°. The DC2 mode does not fit to any results of the calculations and thus cannot yet be assigned.

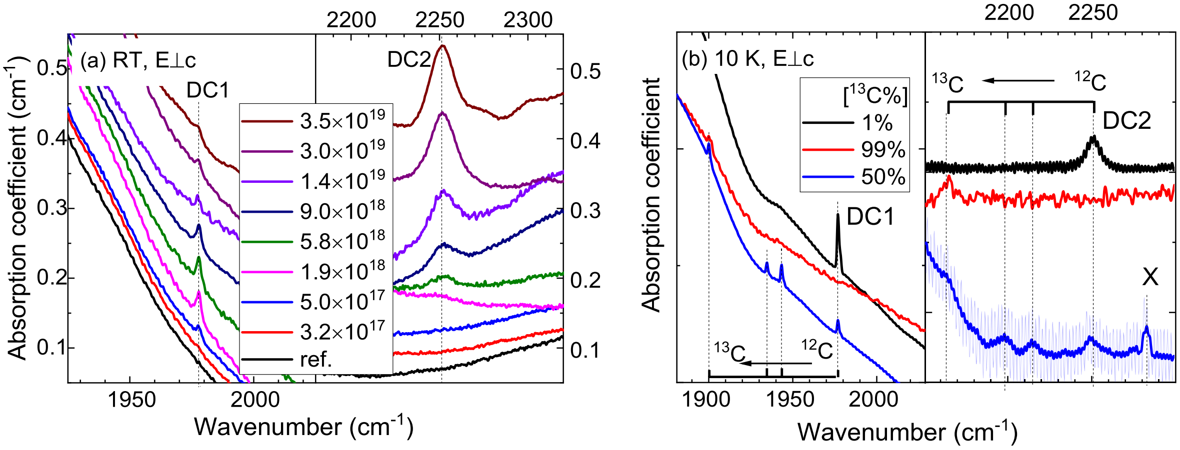

FIG. 6. (a) Uncorrected infrared (IR) absorption spectra in the range of DC1 and DC2 modes for the reference GaN and all 8 GaN:C samples with natural isotope composition at room temperature (RT) for $E\perp c$ polarization. (b) Modes DC1 and DC2 at different isotope abundance: natural $[^{13}\mathrm{C}\,\%] \approx 1\%$ (GaN058), $[^{13}\mathrm{C}\,\%] \approx 50\%$ (GaN051-50), and $[^{13}\mathrm{C}\,\%] \approx 99\%$ (GaN025-99) measured at 10 K for the same polarization. All spectra are shifted vertically for visualization.

C. TC defects

Finally, we turn to the most complex type of carbon defect that is observed in GaN:C, i.e., the vibrations that involve three connected carbon atoms. These defects are labeled as TC. Our previous works showed high prevalence of TC defects in GaN material [18,22,23]. Analysis of the isotope splitting and polarization dependence in GaN:C established the structure of defects covered behind the vibrational modes TC1 and TC2 derived exclusively from the analysis of vibrational spectra [18,22,23]. In this paper, we consider this pair of signals together with their higher-frequency satellites labeled TC3 and TC4 because similar effects are observed for these peaks. Furthermore, we propose a DFT model of TC defects explaining the frequencies of vibration with high accuracy. Mode TC5 appears only at the highest [C] and probably related to similar defects.

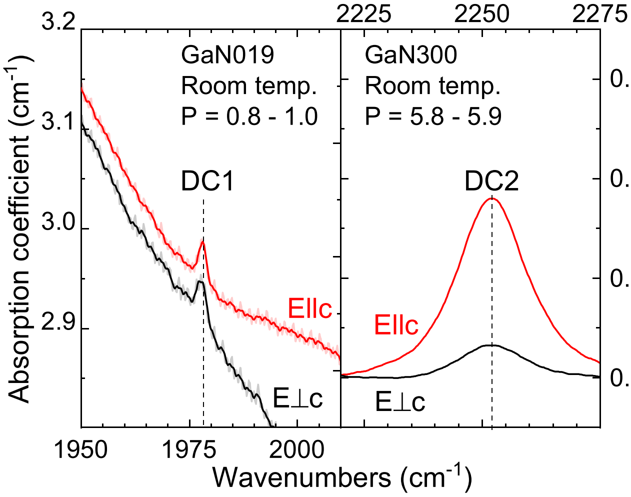

FIG. 7. Infrared (IR) spectra of samples GaN019 (DC1, smoothed) and GaN300 (DC2) for two polarizations $E\perp c$ and $E \parallel c$. Mode DC1 has low intensity nearly equal at both polarizations ($P \approx 0.8$–1.0). Peak DC2 prevails at $E \parallel c$ polarization ($P \approx 5.8$–5.9). The tilt angle of corresponding defects can be evaluated via Eq. (3).

Figure 8(a) shows that the TC1 and TC2 modes at 1673.9 and 1717.8 cm^{-1} from TC defects are still visible for the lowest concentrations of carbon doping within the examined range in this paper (GaN003 with $[\mathrm{C}] = 3.2 \times 10^{17}\ \mathrm{cm}^{-3}$, red line), hence, TC defects have manifested at this relatively low [C]. Figure 8(b) displays the polarization dependence of the IR absorption for $[\mathrm{C}] = 1.4 \times 10^{19}\ \mathrm{cm}^{-3}$. Apparently, the spectra for $E||c$ polarization are dominated by TC2 and TC4, and TC1 and TC3 for the $E\perp c$ polarization. Using Eq. (3), the observed polarization dependence directly shows that the dipole moment of defects vibrating in the TC1 mode is oriented in the basal plane (absorbing only at $E\perp c$ polarization), while the dipole moment of the TC2 vibrational mode has a tilt angle of 33 ° relative to the GaN crystal c axis (absorbing at both polarizations) [22,23].

The structure of complexes in previous theoretical reports [10,14–16] cannot explain the extensive data provided by vibrational spectroscopy [Figs. 9(a)–9(c)]. Using hybrid DFT calculations, in this paper, we discover stable basal and axial configurations of TC complexes [the basal one is shown in Fig. 9(d)]. For the two configurations (basal, axial) of TC defects, DFT provides the symmetric stretching (ν_1) modes at (1165 and 1192 cm^{-1}) and antisymmetric stretching (ν_3) modes at (1671 and 1691 cm^{-1}). As was established in Ref. [22], the TC2 mode is the ν_3 mode of the bent $\mathrm{C}_X{=}\mathrm{C}_Y{=}\mathrm{C}_Z$ triatomic chain of three C atoms ($n = 3$) at three unique structural positions (X, Y, and Z), as confirmed by an eightfold isotopic splitting. This eightfold splitting (labeled TC2-8 to TC2-1) is clearly visible in the GaN051-50 sample in Fig. 9(b). Performing $^{12}\mathrm{C} \rightarrow {}^{13}\mathrm{C}$ isotopic replacement in hybrid DFT calculations (Table III) reproduces the eightfold isotope splitting (in Fig. 9 shown by the stick spectra). The sixfold splitting of TC1 [Fig. 9(c)] indicates a $\mathrm{C}_X{=}\mathrm{C}_Y{=}\mathrm{C}_X$ structure, with symmetrical positions of the outer atoms (Z equal to X) [22]. In DFT, the basal configuration provides only six unique frequencies ν_3 and three unique frequencies ν_1 (Table III). While the sixfold splitting

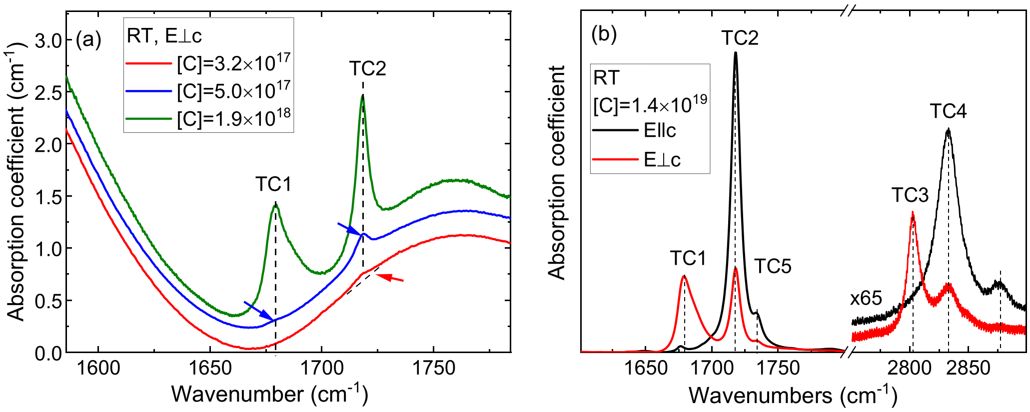

FIG. 8. (a) Infrared (IR) absorption spectra of samples GaN003, GaN005, and GaN019 at room temperature (RT) and $E \perp c$ polarization containing peaks TC1 and TC2. (b) Polarization dependence is shown for sample GaN140. Peaks TC2 and TC4 dominate for $E \parallel c$ polarization but appear at both polarizations, while TC1 and TC3 are detectable at $E \perp c$ polarization only.

emphasizes the symmetry of the basal defect structure [22], the splitting of the ν_1 mode into only three unique frequencies is assigned to additional degeneration caused by the symmetry of the symmetrical vibrational mode and the high values of the angle between the two carbon-carbon bonds. For these two reasons, the vibrational amplitude of the central C atom in the ν_1 mode according to DFT is ∼20 times smaller than for the outer C atoms, explaining the degeneration to three unique ν_1. To summarize, in all listed aspects, the DFT model satisfies experimental observations including $f \approx f_{\max}$ for the complete isotope replacement.

The frequencies in the range of $\nu_3 \sim 1700$ cm^{-1} and the equilibrium distance between the carbon atoms of 0.134 nm are typical for double carbon-carbon (C=C) bonds [49–51]. In contrast, the TC defect with the equilibrium distance 0.148 nm (C_N–C_{Ga}–C_N) reported earlier by Lyons *et al.* [Fig. 9(e)] shows a much lower frequency $\nu_3 \sim 1152$ cm^{-1} and larger bond distances expected for single (C–C) bonds [10,51]. The difference in the bond order appears due to the breaking of the chemical bond between the central C atom and the neighboring nitrogen atom, together with a large deviation of the central C atom from the original position of the substituted Ga atom. The calculations provide an angle of 161 ° between the $C_N = C$ bonds for the basal defects vs 134 ± 8 ° evaluated from the isotope splitting [22]. It is equivalent to the deviation of the central C atom from the position of the substituted Ga atom which is slightly larger in the DFT model than it follows from the isotopic experiment. In this respect, the

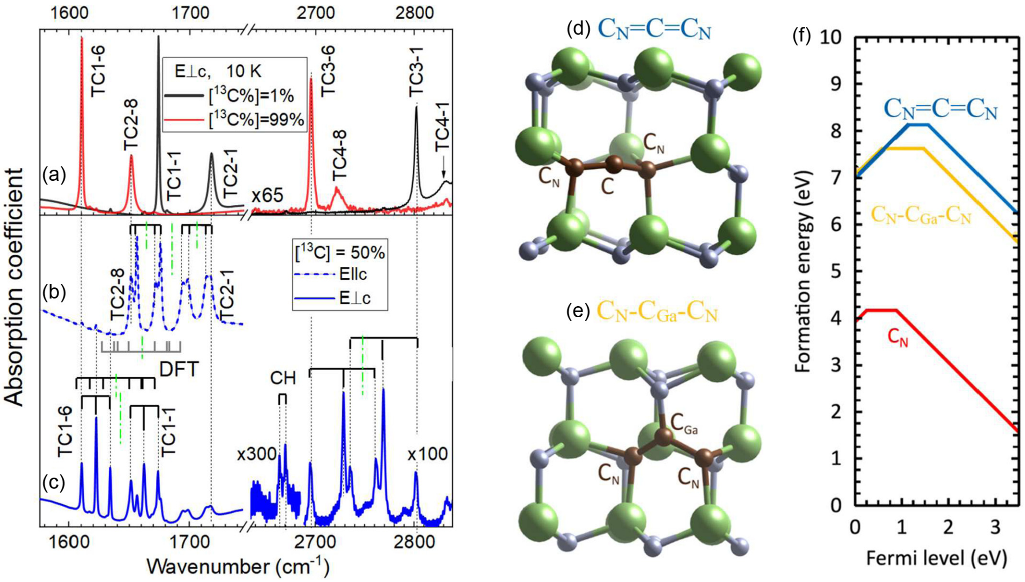

FIG. 9. (a) Infrared (IR) absorption spectra of samples with different isotope ^{13}C abundance [^{13}C %] = 1% (GaN019) and 99% (GaN025-99) for $E \perp c$ polarization. IR absorption spectra of sample GaN051-50 ([^{13}C %] = 50%) for (b) $E \perp c$ and (c) $E \parallel c$ polarizations. The eightfold splitting of TC1 (b) and sixfold splitting of TC2 (c) were discussed in Ref. [22]. The splitting of mode TC3 shown in (c) has identical nature and corresponds to the same triatomic structure. Splitting of the faint mode TC4 could not be observed. All spectra are captured at 10 K. (d) Density functional theory (DFT) model of basal tricarbon (TC) defect found in this paper vibrating at $\nu_3 = 1671$ cm^{-1}. (e) Configuration of basal TC defect reported earlier by Lyons *et al.* [10] and vibrating at $\nu_3 = 1152$ cm^{-1}. (f) Formation energy vs Fermi level for the two configurations of TC complexes compared with C_N [10,13]. Frequencies obtained for TC1 and TC2 via DFT are shown with the stick spectra.

TABLE III. Symmetrical (ν_1), antisymmetrical (ν_3), and combination ($\nu_1 + \nu_3$) vibrational mode frequencies of different isotopomers obtained from IR absorption spectra at 10 K and from DFT.

	Frequency of basal TC defect, cm^{-1}							Frequency of axial TC defect, cm^{-1}						
	ν_3			$(\nu_1 + \nu_3)$		ν_1		ν_3			$(\nu_1 + \nu_3)$		ν_1	
Isotopomer	Peak TC1	Exp.	DFT	Peak TC3	Exp.	Exp.[a]	DFT	Peak TC2	Exp.	DFT	Peak TC4	Exp.	Exp.[a]	DFT
$^{12}\text{C}-^{12}\text{C}-^{12}\text{C}$	1	1673.9	1671	1	2803.5	~1130	1165	1	1717.8	1692	1	2831	~1115	1182
$^{13}\text{C}-^{12}\text{C}-^{12}\text{C}$	2	1662.3	1661	2	2769.3	~1107	1142	2	1714.4	1683	–	–	–	1158
$^{12}\text{C}-^{12}\text{C}-^{13}\text{C}$			1660				1142	3	1699.0	1681	–	–	–	1160
$^{13}\text{C}-^{12}\text{C}-^{13}\text{C}$	3	1651.5	1650	3	2736.7	~1085	1120	4	1694.6	1671	–	–	–	1137
$^{12}\text{C}-^{13}\text{C}-^{12}\text{C}$	4	1634.1	1628	4	2760.6	~1127	1164	5	1675.8	1649	–	–	–	1181
$^{13}\text{C}-^{13}\text{C}-^{12}\text{C}$	5	1622.5	1617	5	2729.0	~1107	1142	6	1672.4	1640	–	–	–	1157
$^{12}\text{C}-^{13}\text{C}-^{13}\text{C}$			1617				1142	7	1656.5	1637	–	–	–	1159
$^{13}\text{C}-^{13}\text{C}-^{13}\text{C}$	6	1610.5	1606	6	2695.0	~1085	1120	8	1651.7	1627	8	2721	~1069	1136

[a] Obtained from corresponding value of $(\nu_1 + \nu_3)$, without anharmonic correction.

configurations can be labeled as $\text{C}_\text{N}{=}\text{C}{=}\text{C}_\text{N}$, emphasizing the difference from the $\text{C}_\text{N}\text{–C}_\text{Ga}\text{–C}_\text{N}$ configuration from the earlier report.

Although the frequencies of the vibrational modes TC3 and TC4 lie in the typical range of carbon-hydrogen vibrations, the isotopic effects clearly exclude C–H as the origin of TC3 and TC4. The isotopic effects observed for TC3 and TC4 include the splitting to six individual frequencies with frequency ratio $f \approx 1.0400 \pm 0.0005$, identical to the value found for TC1 and TC2 and close to f_max. Furthermore, the sixfold splitting to two symmetrical 1:2:1 triplets [Fig. 9(c)] for TC3 (like one observed for TC1) indicates $\text{C}_X{=}\text{C}_Y{=}\text{C}_X$ structure of the defect [22]. In this respect, TC3 and TC4 modes at 2802 and 2833 cm^{-1} can be considered as combination vibration $(\nu_1 + \nu_3)$ of $\text{C}_\text{N}{=}\text{C}{=}\text{C}_\text{N}$ defects with frequencies close to their algebraic sum of the basic modes ν_1 and ν_3. One can compare $\text{C}_\text{N}{=}\text{C}{=}\text{C}_\text{N}$ defects in GaN with the laser-ablated TC clusters vibrating at ν_3 equal to 2040 or 1722 cm^{-1} (for two different configurations) [49,50]. The combination vibration $(\nu_1 + \nu_3)$ of one of the configurations of such clusters are found experimentally at 3250 cm^{-1} with anharmonicity <10 cm^{-1} [49,50]. Then the vibration frequency ν_1 for the basal $\text{C}_\text{N}{=}\text{C}{=}\text{C}_\text{N}$ defect can be evaluated as ~1130 cm^{-1} (as the difference between TC1 and TC3 without considering the anharmonicity effect) [49]. Thus, our DFT model overestimates ν_1 (1165 cm^{-1}, Table III) by ~1% which can be regarded as good agreement.

We have also calculated the optical properties of the $\text{C}_\text{N}{=}\text{C}{=}\text{C}_\text{N}$ complex for comparison with the results obtained for the $\text{C}_\text{N}\text{–C}_\text{Ga}\text{–C}_\text{N}$ complex in Ref. [10]. Despite the distinct structural configuration, the (0/−) transition of $\text{C}_\text{N}{=}\text{C}{=}\text{C}_\text{N}$ (involving recombination from a state in the conduction band) features a similar ZPL of 1.93 eV, with a relaxation energy of 0.50 eV and a resulting predicted PL peak of 1.43 eV (cf. 2.00 eV ZPL and 1.56 eV PL for $\text{C}_\text{N}\text{–C}_\text{Ga}\text{–C}_\text{N}$) [10]. Thus, the two configurations in the negative charge state are difficult to distinguish based on optical experiments alone, but it is possible that TC defects could be responsible for the emission band ~1.62 eV for $[\text{C}] > 10^{18}$ cm^{-3} reported earlier for the same sample set [24]. For the (0/+) transition, in contrast, the ZPL and PL energies of the $\text{C}_\text{N}{=}\text{C}{=}\text{C}_\text{N}$ defect are equal to 2.34 and 1.85 eV and are 0.6 eV less than the corresponding values for $\text{C}_\text{N}\text{–C}_\text{Ga}\text{–C}_\text{N}$ [10]. We note that, due to this difference, $(\text{C}_\text{N}{=}\text{C}{=}\text{C}_\text{N})^+$ becomes a compensating defect for C_N^- since now the ZPL (0/+) of $\text{C}_\text{N}{=}\text{C}{=}\text{C}_\text{N}$ is located at 0.2 eV closer to the conduction band than the ZPL (0/−) of C_N defects.

The diagram in Fig. 9(f) compares formation energies as a function of the Fermi level for $\text{C}_\text{N}{=}\text{C}{=}\text{C}_\text{N}$, $\text{C}_\text{N}\text{–C}_\text{Ga}\text{–C}_\text{N}$, and C_N. Both TC complexes are significantly higher in energy than C_N, other defects with one carbon atom, or carbon pair complexes [10]. Although for most Fermi levels the formation energy of the $\text{C}_\text{N}{=}\text{C}{=}\text{C}_\text{N}$ complex is ~0.5 eV higher than for the $\text{C}_\text{N}\text{–C}_\text{Ga}\text{–C}_\text{N}$ configuration, it is nevertheless slightly more stable when the Fermi level is near the VBM [as shown in Fig. 9(f)]. Based solely on formation energies, one would not expect the TC complexes to incorporate in GaN. In contrast, the direct comparison of IR absorption intensities of the peaks (MC2; TC1; TC2) demonstrates prevalence of $\text{C}_\text{N}{=}\text{C}{=}\text{C}_\text{N}$ in most of the samples. Hereby, intensities are equal to 28, 20.2, and 12.7 cm^{-2} at $[\text{C}] = 1.9 \times 10^{18}$ cm^{-3} and increase up to 119, 182, and 93 cm^{-2} at $[\text{C}] = 9 \times 10^{18}$ cm^{-3}. The pronounced incorporation of $\text{C}_\text{N}{=}\text{C}{=}\text{C}_\text{N}$ complexes could be governed by surface kinetic effects not captured within the equilibrium condition of the bulk crystal considered by DFT. Additionally, while the incomplete decomposition of precursors at the growth interface may be another explanation, samples grown with both butane and pentane result in the same pronounced TC modes. Furthermore, our spectroscopic research [52] of the set of HVPE GaN samples grown at Institute of High Pressure Physics (Warsaw, Poland) [44,53,54] and doped with an ethane precursor (i.e., without TC chains in the structure of the precursor molecules) indicates that the intensity of TC signals of $\text{C}_\text{N}{=}\text{C}{=}\text{C}_\text{N}$ defects is the same or even higher relative to the intensity modes MC1–MC4 associated with C_N.

To summarize, models of TC defects in the $\text{C}_\text{N}{=}\text{C}{=}\text{C}_\text{N}$ configuration are in excellent agreement with the observed vibrational properties. Figure 9(f) illustrates that $\text{C}_\text{N}{=}\text{C}{=}\text{C}_\text{N}$ defects exhibit different charge states (from 1+ to 1−) depending on the Fermi level position. The thermodynamic transition levels of $\text{C}_\text{N}{=}\text{C}{=}\text{C}_\text{N}$ defects are closer to midgap than for C_N; the (0/−) level occurs at ~1.5 eV as opposed to 0.9 eV for C_N, while (+/0) is located at 1.1 and ~0.2 eV

TABLE IV. The labels of peaks, detection method (R = Raman, IR = infrared absorption), experimental and theoretical vibrational frequencies, and the frequency ratio f for the six point defects discussed in this paper.

Group	Defect	Label	Method	Experiment		DFT		Comment
				ν, cm^{-1}	f	ν, cm^{-1}	f	
Mono-C	C_N	MC1	R	766	1.028	775	1.030	Fig. 3(a)
		MC2	IR/R	774	1.028	785	1.030	Fig. 3(b)
		MC3	R	659	1.00	655	1.00	Fig. 3(c)
		MC4	R	673	1.00	662	1.0	Fig. 3(d)
		MC5	IR/R	1540	1.028	1570[a]	–	MC2 second harmonics
		MC6	IR/R	1547	1.028	1570[a]	–	
	C–H	CH	IR	2670	1.002	2794[b]	–	Stretching mode C_N–H
Di-C	C_N–C_i	DC1	IR/R	1978	1.040	2057 [10]	–	Stretching mode, tilt angle ∼55°
	C ≡ C?	DC2	IR	2250	1.040	–	–	Stretching mode, tilt angle ∼30°
Tri-C	C_N=C=C_N	TC1	IR	1678	1.040	1671	1.040	Basal config., Fig. 9(e), (ν_3)
		TC2	IR/R	1718	1.040	1692	1.040	Axial config., (ν_3)
		TC3	IR	2803	1.040	2836[a]	1.040	Basal config., ($\nu_1 + \nu_3$)
		TC4	IR	2832	1.040	2874[a]	1.040	Axial config., ($\nu_1 + \nu_3$)
	C=C=C?	TC5	IR	1734	1.040	–	–	Another TC defect?

[a] The algebraic sum of corresponding first-order modes not considering anharmonic effects.
[b] See Sec. III A (CH defects) to clarify the specific in DFT calculations in this case.

above VBM, respectively, for these defects. At Fermi level positions from 0.9 to 1.1 eV above VBM [including the Fermi level pinned to C_N (0/−) or C_N=C=C_N (+/0)], calculations of the C_N=C=C_N defect predict that the 1+ charge state is stable, indicating that $(C_N{=}C{=}C_N)^+$ could compensate negatively charged C_N. Since the intensity of vibrational peaks for these TC centers is one order of magnitude stronger than for other defects, C_N=C=C_N defects should be considered as an important compensating defect in GaN.

D. Summary of carbon-related vibrational modes and behavior under illumination

Table IV summarizes 14 vibrational frequencies which we associate with six different carbon-containing defects [C_N, C–H, C_N–C_i, C≡C, and C_N=C=C_N (basal and axial)]. Table IV includes the vibrational frequencies observed in experiments (IR absorption or Raman) and those obtained from DFT calculations. The frequency ratios f obtained from the experiments and DFT calculations are shown. For the most pronounced signals of C_N and C_N=C=C_N defects, we refer to the illustrations provided above, while for faint vibrational modes, we restrict ourselves to the verbal description. Even within the set of samples grown by HVPE in similar conditions, the relation between signals of the defects is distinct at different [C], as shown in Fig. 10. Axial C_N=C=C_N defects (TC2) were found in the sample with the lowest doping level, which emphasizes their high prevalence in GaN:C. The vibrational modes of C_N defects (MC1–MC4), however, dominate among the other Raman-active defect-related signals. In this respect, we suggest considering both C_N (at all [C]) and TC (at medium and high [C]) as dominating defects. We also note that excitation >2.5 eV [in the range of the defect related ultraviolet-visible (UV-Vis) absorption] [23] leads to a significant gain in sensitivity in the scattering experiments. Comparing with earlier reports in which excitation at 532 nm (2.33 eV) was used in Raman experiments [11,26], we get reliable signal detection

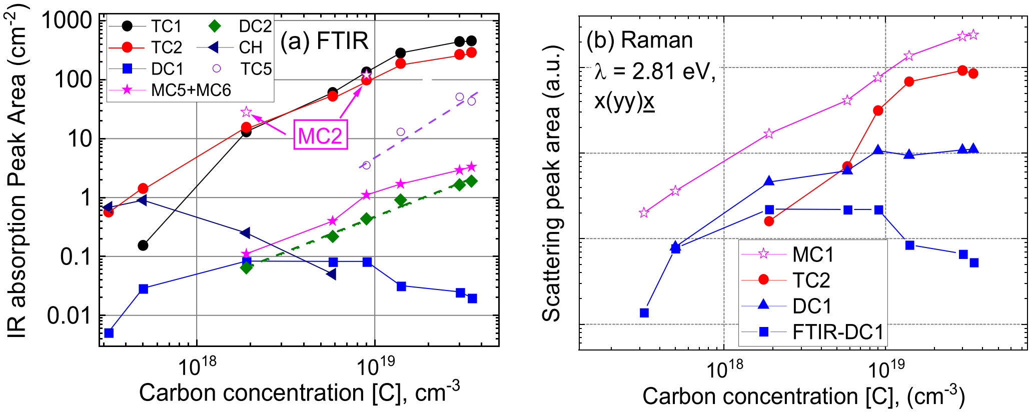

FIG. 10. Integrated peak areas of different vibrational modes at different [C] at room temperature obtained from (a) infrared (IR) absorption spectra at $E \perp c$ polarization and (b) Raman scattering spectra at 2.81 eV excitation in $x(yy)\underline{x}$ geometry. Fourier transform IR (FTIR)-DC1 signal is reproduced in (b) for comparison with the corresponding Raman mode DC1 (normalized to the value at [C] = 5 × 10^{17} cm^{-3}).

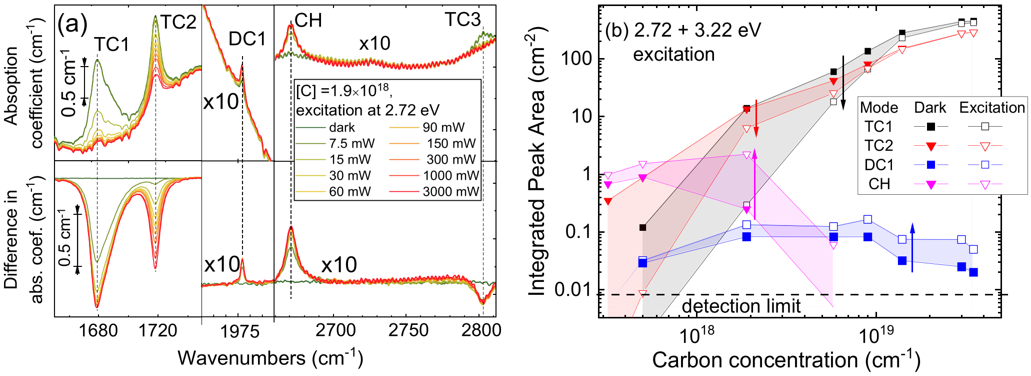

FIG. 11. (a) Infrared (IR) absorption spectra of sample with [C] of 1.9×10^{18} cm^{-3} for $E \perp c$ polarization at room temperature and different powers of additional excitation at 2.72 eV. (b) Integrated peak area of different IR absorption peaks at different [C] obtained at combined excitation of 2.72 and 3.22 eV with total power of 4500 mW (optical power of the LEDs, coupling losses are not accounted).

at 1–2 orders of magnitude lower [C]. In our experiments, C_N begins to appear at [C] = 3.2×10^{17} cm^{-3}.

Note that the relative intensity of the signals is significantly different when using FTIR spectroscopy [Fig. 10(a)] and Raman spectroscopy [Fig. 10(b)] since the incident laser light in the Raman experiments puts the samples into an excited state. The vibrational intensities of photosensitive defects in this case change, and this effect can be observed independently in FTIR experiments with additional light excitation. Figure 11(a) shows the IR absorption spectra of the most sensitive sample at [C] = 1.9×10^{18} cm^{-3} in the dark and under additional excitation at varied power of a 2.71 eV LED during the measurement of IR absorption. The detector of the IR spectrometer is insensitive to this irradiation; we also may exclude the heating of the samples, as the temperature-dependent peaks do not change the spectral position and shape.

The optical absorption increases in the sample set at the excitation wavelength from 5 to 20 cm^{-1} with increasing [C]; hence, to stimulate the changes of the defects more effectively, we include the excitation at 3.22 eV (absorption is $5 \cdots 500$ cm^{-1} depending on [C]) [22,23]. This excitation, in contrast, has low penetration depth in samples with high [C]. In this respect, the combined excitation (2.71 and 3.22 eV simultaneously) is used for comparison of samples with different [C] [summarized in Fig. 11(b)]. The temperature-sensitive mode TC1 does not change its spectral position or width, so we exclude significant heating of the crystals during the excitation.

Under the excitation at 2.71 eV (or/and 3.22 eV), the signals MC5 and MC6 (not shown), TC1, TC2, TC3, and TC4 decrease in intensity, while DC1 and CH become far more pronounced. In addition, CH defects can be present in crystals in the IR inactive state since they are not found in the dark at [C] = 5.8×10^{18} cm^{-3} but appear under excitation [Fig. 11(b)]. A change in the intensity of vibrational modes can be caused by a change in the defect population (i.e., their charge state changes) or in the structural configuration of these defects. The duration of these processes depends on [C] (and is faster at higher [C]) and ranges from a few seconds to a few minutes. Similar timeframes are typical for the charge transfer observed by Zvanut *et al.* [19,53] or for the bulk photovoltaic effect observed by Levine, Gamov *et al.* [20] in C-doped GaN. One of the mechanisms explaining the simultaneous change of several vibrational modes can be the band-mediated transfer of charge carriers between donor defect and acceptor defect levels, which brings the crystal system out of equilibrium into a metastable excited state [55].

IV. CONCLUSIONS

In conclusion, six types of carbon-containing defects were observed by methods of vibrational spectroscopy. The structure of these defects was established via isotope-mass effects analyzed within DFT calculations as well as in the harmonic oscillator approximation for localized vibrational modes. C_N and $C_N{=}C{=}C_N$ were identified as pronounced defects with clear signatures in the vibrational spectra, and the fraction of $C_N{=}C{=}C_N$ increases at high [C]. In Raman experiments, the excitation in the range of defect absorption provided the confident detection of C_N defects even at [C] as low as 3.2×10^{17} cm^{-3}. $C_N{=}C{=}C_N$ complexes are observed at the same [C] in IR absorption spectra despite their high formation energies from DFT calculations. According to our calculations, these two defects could explain self-compensation during carbon doping in GaN if the Fermi level position is pinned between the C_N (0/−) and $C_N{=}C{=}C_N$ (+/0) transition levels. This supports the suggestion that, at [C], in the order of 10^{18} cm^{-3} and higher, when the fraction of TC defects visibly rises, $C_N{=}C{=}C_N$ defects can compensate the negatively charged C_N defects. Other defects, such as CH groups and carbon pairs, are faint in the vibrational spectra of our HVPE crystals but can probably be more prominent for other growth methods, stoichiometry Ga/N, or co-doping. Furthermore, DC1 and CH signals are enhanced by UV-Vis irradiation; therefore, the corresponding defects can exist in the crystal but not appear in the vibrational spectra. Note the importance of these defects—defects showing changes in vibrational mode intensity at additional excitation during FTIR experiments (MC5, MC6, DC1, TC1–TC6, and CH) presumably impact the electronic charge balance and thus the conductivity of the material.

ACKNOWLEDGMENTS

The authors are glad to mention the influence of Prof. Dr. Axel Hoffman and Dr. Harald Scheel from TU Berlin and appreciate their help with the experiments and valuable discussion. I.G. thanks Institute of High Pressure Physics of the Polish Academy of Sciences and Prof. Dr. M. Bockowski. Support for work at NRL was provided by the Office of Naval Research/NRL Basic Research Program, and DFT calculations were supported by the U.S. Department of Defence High Performance Computing Modernization Program at the U.S. Army Engineer Research and Development Center.

---

[1] H. Amano, Y. Baines, E. Beam, M. Borga, T. Bouchet, P. R. Chalker, M. Charles, K. J. Chen, N. Chowdhury, R. Chu *et al.*, The 2018 GaN power electronics roadmap, J. Phys. D. Appl. Phys. **51**, 163001 (2018).

[2] S. Kato, Y. Satoh, H. Sasaki, I. Masayuki, and S. Yoshida, C-doped GaN buffer layers with high breakdown voltages for high-power operation AlGaN/GaN HFETs on 4-in Si substrates by MOVPE, J. Cryst. Growth **298**, 831 (2007).

[3] E. Bahat-Treidel, F. Brunner, O. Hilt, E. Cho, J. Wurfl, and G. Tränkle, AlGaN/GaN/GaN:C back-barrier HFETs with breakdown voltage of over 1 kV and low $R_{ON} \times A$, IEEE Trans. Electron Devices **57**, 3050 (2010).

[4] A. Fariza, A. Lesnik, J. Bläsing, M. P. Hoffmann, F. Hörich, P. Veit, H. Witte, A. Dadgar, and A. Strittmatter, On reduction of current leakage in GaN by carbon-doping, Appl. Phys. Lett. **109**, 212102 (2016).

[5] A. E. Wickenden, D. D. Koleske, R. L. Henry, M. E. Twigg, and M. Fatemi, Resistivity control in unintentionally doped GaN films grown by MOCVD, J. Cryst. Growth **260**, 54 (2004).

[6] C. Ozgit-Akgun, E. Goldenberg, A. K. Okyay, and N. Biyikli, Hollow cathode plasma-assisted atomic layer deposition of crystalline AlN, GaN and $Al_xGa_{1-x}N$ thin films at low temperatures, J. Mater. Chem. C **2**, 2123 (2014).

[7] C. H. Seager, A. F. Wright, J. Yu, and W. Götz, Role of carbon in GaN, J. Appl. Phys. **92**, 6553 (2002).

[8] D. D. Koleske, A. E. Wickenden, R. L. Henry, and M. E. Twigg, Influence of MOVPE growth conditions on carbon and silicon concentrations in GaN, J. Cryst. Growth **242**, 55 (2002).

[9] J. L. Lyons, A. Janotti, and C. G. Van De Walle, Carbon impurities and the yellow luminescence in GaN, Appl. Phys. Lett. **97**, 152108 (2010).

[10] J. L. Lyons, E. R. Glaser, M. E. Zvanut, S. Paudel, M. Iwinska, T. Sochacki, and M. Bockowski, Carbon complexes in highly C-doped GaN, Phys. Rev. B **104**, 075201 (2021).

[11] S. Wu, X. Yang, H. Zhang, L. Shi, Q. Zhang, Q. Shang, Z. Qi, Y. Xu, J. Zhang, N. Tang *et al.*, Unambiguous Identification of Carbon Location on the N Site in Semi-Insulating GaN, Phys. Rev. Lett. **121**, 145505 (2018).

[12] M. A. Reshchikov, M. Vorobiov, D. O. Demchenko, Ü. Özgür, H. Morkoç, A. Lesnik, M. P. Hoffmann, F. Hörich, A. Dadgar, and A. Strittmatter, Two charge states of the C_N acceptor in GaN: Evidence from photoluminescence, Phys. Rev. B **98**, 125207 (2018).

[13] J. L. Lyons, A. Janotti, and C. G. Van de Walle, Effects of carbon on the electrical and optical properties of InN, GaN, and AlN, Phys. Rev. B **89**, 035204 (2014).

[14] M. Matsubara and E. Bellotti, A first-principles study of carbon-related energy levels in GaN. I. Complexes formed by substitutional/interstitial carbons and gallium/nitrogen vacancies, J. Appl. Phys. **121**, 195701 (2017).

[15] M. Matsubara and E. Bellotti, A first-principles study of carbon-related energy levels in GaN. II. Complexes formed by carbon and hydrogen, silicon or oxygen, J. Appl. Phys. **121**, 195702 (2017).

[16] P. Deák, M. Lorke, B. Aradi, and T. Frauenheim, Carbon in GaN: Calculations with an optimized hybrid functional, Phys. Rev. B **99**, 085206 (2019).

[17] A. Lesnik, M. P. Hoffmann, A. Fariza, J. Bläsing, H. Witte, P. Veit, F. Hörich, C. Berger, J. Hennig, A. Dadgar *et al.*, Properties of C-doped GaN, Phys. Status Solidi **254**, 1600708 (2017).

[18] E. Richter, F. C. Beyer, F. Zimmermann, G. Gärtner, K. Irmscher, I. Gamov, J. Heitmann, M. Weyers, and G. Tränkle, Growth and properties of intentionally carbon-doped GaN layers, Cryst. Res. Technol. **55**, 1900129 (2019).

[19] M. E. Zvanut, S. Paudel, U. R. Sunay, W. R. Willoughby, M. Iwinska, T. Sochacki, and M. Bockowski, Charge transfer process for carbon-related center in semi-insulating carbon-doped GaN, J. Appl. Phys. **124**, 075701 (2018).

[20] I. Levine, I. Gamov, M. Rusu, K. Irmscher, C. Merschjann, E. Richter, M. Weyers, and T. Dittrich, Bulk photovoltaic effect in carbon-doped gallium nitride revealed by anomalous surface photovoltage spectroscopy, Phys. Rev. B **101**, 245205 (2020).

[21] T. Kogiso, T. Narita, H. Yoshida, Y. Tokuda, K. Tomita, and T. Kachi, Characterization of hole traps in MOVPE-grown *p*-type GaN layers using low-frequency capacitance deep-level transient spectroscopy, Jpn. J. Appl. Phys. **58**, SCCB36 (2019).

[22] I. Gamov, E. Richter, M. Weyers, G. Gärtner, and K. Irmscher, Carbon doping of GaN: Proof of the formation of electrically active tri-carbon defects, J. Appl. Phys. **127**, 205701 (2020).

[23] K. Irmscher, I. Gamov, E. Nowak, G. Gärtner, F. Zimmermann, F. C. Beyer, E. Richter, M. Weyers, and G. Tränkle, Tri-carbon defects in carbon doped GaN, Appl. Phys. Lett. **113**, 262101 (2018).

[24] F. Zimmermann, J. Beyer, F. C. Beyer, G. Gärtner, I. Gamov, K. Irmscher, E. Richter, M. Weyers, and J. Heitmann, A carbon-doping related luminescence band in GaN revealed by below bandgap excitation, J. Appl. Phys. **130**, 055703 (2021).

[25] D. O. Demchenko, I. C. Diallo, and M. A. Reshchikov, Hydrogen-carbon complexes and the blue luminescence band in GaN, J. Appl. Phys. **119**, 035702 (2016).

[26] M. F. Cerqueira, L. G. Vieira, A. Alves, R. Correia, M. Huber, A. Andreev, A. Bonanni, and M. I. Vasilevskiy, Raman and IR-ATR spectroscopy studies of heteroepitaxial structures with a GaN:C top layer, J. Phys. D. Appl. Phys. **50**, 365103 (2017).

[27] S. Ito, H. Kobayashi, K. Araki, K. Suzuki, N. Sawaki, K. Yamashita, Y. Honda, and H. Amano, Resonant Raman and FTIR spectra of carbon doped GaN, J. Cryst. Growth **414**, 56 (2015).

[28] C. Freysoldt, B. Grabowski, T. Hickel, J. Neugebauer, G. Kresse, A. Janotti, and C. G. Van de Walle, First-principles calculations for point defects in solids, Rev. Mod. Phys. **86**, 253 (2014).

[29] P. E. Blöchl, Projector augmented-wave method, Phys. Rev. B **50**, 17953 (1994).

[30] G. Kresse and J. Furthmüller, Efficient iterative schemes for *ab initio* total-energy calculations using a plane-wave basis set, Phys. Rev. B **54**, 11169 (1996).

[31] J. Heyd and G. E. Scuseria, Efficient hybrid density functional calculations in solids: Assessment of the Heyd-Scuseria-Ernzerhof screened Coulomb hybrid functional, J. Chem. Phys. **121**, 1187 (2004).

[32] J. Heyd, G. E. Scuseria, and M. Ernzerhof, Erratum: "Hybrid functionals based on a screened Coulomb potential" [J. Chem. Phys. 118, 8207 (2003)], J. Chem. Phys. **124**, 219906 (2006).

[33] J. M. Zhang, T. Ruf, M. Cardona, O. Ambacher, M. Stutzmann, J.-M. Wagner, and F. Bechstedt, Raman spectra of isotopic GaN, Phys. Rev. B **56**, 14399 (1997).

[34] U. Haboeck, H. Siegle, A. Hoffmann, and C. Thomsen, Lattice dynamics in GaN and AlN probed with first- and second-order Raman spectroscopy, Phys. Status Solidi **0**, 1710 (2003).

[35] V. Yu. Davydov, Yu. E. Kitaev, I. N. Goncharuk, A. M. Tsaregorodtsev, A. N. Smirnov, A. O. Lebedev, V. M. Botnaryk, Yu. V. Zhilyaev, M. B. Smirnov, A. P. Mirgorodsky *et al.*, Phonon spectrum of wurtzite GaN and AlN, J. Cryst. Growth **189–190**, 656 (1998).

[36] J. Yang, G. J. Brown, M. Dutta, and M. A. Stroscio, Photon absorption in the Restrahlen band of thin films of GaN and AlN: Two phonon effects, J. Appl. Phys. **98**, 043517 (2005).

[37] K. Irmscher, C. Hartmann, C. Guguschev, M. Pietsch, J. Wollweber, and M. Bickermann, Identification of a tri-carbon defect and its relation to the ultraviolet absorption in aluminum nitride, J. Appl. Phys. **114**, 123505 (2013).

[38] H. C. Alt, H. E. Wagner, A. Glacki, C. Frank-Rotsch, and V. Häublein, Isotopic study of mid-infrared vibrational modes in GaAs related to carbon and nitrogen impurities, Phys. Status Solidi **252**, 1827 (2015).

[39] C. Künneth, S. Kölbl, H. E. Wagner, V. Häublein, A. Kersch, and H. C. Alt, Symmetry and structure of carbon-nitrogen complexes in gallium arsenide from infrared spectroscopy and first-principles calculations, J. Appl. Phys. **123**, 161553 (2018).

[40] I. Gamov, C. Hartmann, J. Wollweber, A. Dittmar, T. Straubinger, M. Bickermann, I. Kogut, H. Fritze, and K. Irmscher, Carbon pair defects in aluminum nitride, J. Appl. Phys. **126**, 215102 (2019).

[41] A. Kaschner, H. Siegle, G. Kaczmarczyk, M. Straßburg, A. Hoffmann, C. Thomsen, U. Birkle, S. Einfeldt, and D. Hommel, Local vibrational modes in Mg-doped GaN grown by molecular beam epitaxy, Appl. Phys. Lett. **74**, 3281 (1999).

[42] A. Nikolenko, V. Strelchuk, B. Tsykaniuk, D. Kysylychyn, G. Capuzzo, and A. Bonanni, Resonance Raman spectroscopy of Mn-Mg$_k$ cation complexes in GaN, Crystals **9**, 235 (2019).

[43] W. Limmer, W. Ritter, R. Sauer, B. Mensching, C. Liu, and B. Rauschenbach, Raman scattering in ion-implanted GaN, Appl. Phys. Lett. **72**, 2589 (1998).

[44] M. Amilusik, M. Zajac, T. Sochacki, B. Lucznik, M. Fijalkowski, M. Iwinska, D. Wlodarczyk, A. K. Somakumar, A. Suchocki, and M. Bockowski, Carbon and manganese in semi-insulating bulk GaN crystals, Materials **15**, 2379 (2022).

[45] B. R. Davidson, R. C. Newman, T. J. Bullough, and T. B. Joyce, Dynamics of the H-C$_{As}$, complex in GaAs, Phys. Rev. B **48**, 17106 (1993).

[46] B. Clerjaud, D. Côte, W. Hahn, and W. Ulrici, Carbon-hydrogen complex in GaP, Appl. Phys. Lett. **58**, 1860 (1998).

[47] S. Limpijumnong, J. E. Northrup, and C. G. Van de Walle, Identification of hydrogen configurations in *p*-type GaN through first-principles calculations of vibrational frequencies, Phys. Rev. B **68**, 075206 (2003).

[48] G. Herzberg, *Molecular Spectra and Molecular Structure, II. Infrared and Raman Spectra of Polyatomic Molecules* (D. van Nostrand, New York, 1949).

[49] J. Szczepanski and M. Vala, The $\nu_1 + \nu_3$ combination mode of C$_3$ in Ar and Kr matrices: evidence for a bent structure, J. Chem. Phys. **99**, 7371 (1993).

[50] J. Szczepanski, C. Wehlburg, and M. Vala, C$_3$-carbon cluster anion: structure and asymmetric stretching mode frequency, J. Phys. Chem. A **101**, 7039 (1997).

[51] E. A. Robinson and M. W. Lister, A linear relationship between bond orders and stretching force constants, Can. J. Chem. **41**, 2988 (1963).

[52] I. Gamov, Spectral signatures and properties of carbon defects in GaN and AlN, doctoral thesis, Technical University Berlin, 2022.

[53] M. E. Zvanut, S. Paudel, E. R. Glaser, M. Iwinska, T. Sochacki, and M. Bockowski, Incorporation of carbon in free-standing HVPE-grown GaN substrates, J. Electron. Mater. **48**, 2226 (2019).

[54] M. Iwinska, R. Piotrzkowski, E. Litwin-Staszewska, T. Sochacki, M. Amilusik, M. Fijalkowski, B. Lucznik, and M. Bockowski, Highly resistive C-doped hydride vapor phase epitaxy-GaN grown on ammonothermally crystallized GaN seeds, Appl. Phys. Express **10**, 011003 (2017).

[55] I. Gamov, C. Hartmann, T. Straubinger, and M. Bickermann, Photochromism and influence of point defect charge states on optical absorption in aluminum nitride (AlN), J. Appl. Phys. **129**, 113103 (2021).